Microstructure characterisation and mechanical properties of a functionally-graded NbC/high chromium white cast iron composite

Kan, W. H., Albino, C., Dias-da-Costa, D., et al.

Abstract

A functionally graded NbC – high chromium white cast iron composite was successfully fabricated by centrifugal casting for high wear applications. The migration of primary NbC particles to the outer periphery, as predicted by Stokes' law, resulted in an extremely hard outer layer at the surface of a softer bulk material. Microstructural characterisation showed that both the volume fraction and the morphology of the carbides varies along the thickness of the specimen. At the outer surface, the NbC was present as primary carbides while Chinese-script NbC was found in the bulk of the material. Hardness, sliding wear and three-point bending tests confirmed that the outer layer was harder and more wear resistant than the rest of the material, which was correspondingly tougher. The study of the fracture surface of the specimens showed that there is a strong bond between NbC and the matrix such that delamination between the reinforcements and the matrix did not occur during fracture. If Chinese-script NbC can be reduced or prevented in the bulk material, further improvements to toughness could be achieved.

1. Introduction

A functionally-graded metal matrix composite (FGMMC) is an advanced class of composite materials that contains variations in the morphology and volume fraction of ceramic particles throughout a host metal matrix, resulting in differences in the mechanical properties across the material. Centrifugal casting is a common FGMMC fabrication method that takes advantage of Stokes' law, namely, by utilising centrifugal forces to distribute ceramic particles suspended in a molten metal during the casting process [1-3]. Each ceramic particle will thus experience a centrifugal force and an opposing viscous drag force, which can be expressed by Equation (1),

$$m_p \frac{d^2r}{dt^2} = \left|\rho_p - \rho_m\right| \frac{4}{3} \pi \left(\frac{D_p}{2}\right) G_g - 3\pi\eta D_p \frac{dr}{dt} \qquad (1)$$

where dr/dt, d^2r/dt^2, m, ρ, g, D, and η are velocity (in the radial direction), acceleration, mass, density, gravitational acceleration, particle diameter and the viscosity of the molten metal, respectively, with the subscripts 'p' and 'm' denoting particle and metal, respectively [1, 2, 4].

Following on from Equation (1), with the centrifugal casting parameters held equal, the denser the ceramic phase is with respect to the molten metal (represented by $\rho_p - \rho_m$), or the larger the ceramic particle size is (D_p), the greater the tendency for it to migrate towards the outer periphery of the casting. However, as these particles migrate radially

Kan, W. H., Albino, C., Dias-da-Costa, D., et al., Microstructure characterisation and mechanical properties of a functionally-graded NbC/high chromium white cast iron composite, Materials Characterization, Elsevier, 136, 196–205, 2018 (doi: 10.1016/j.matchar.2017.12.020).

toward the outermost periphery, there will also be an accompanying increase in the effective melt viscosity. Once the viscosity at the outermost periphery reaches a certain point, which corresponds to a particular volume fraction of ceramic particles known as the *maximum packing fraction* [4], further migration of ceramic particles to this region will be limited and subsequent particles will simply "settle" above this region. This process will then continue until all ceramic particles have fully migrated outwardly as far as possible, ultimately forming a gradient of ceramic particle volume fractions across the entire material (i.e. an FGMMC). Since Equation (1) does not account for a change in melt viscosity (η), Brinkman's equation can be used to compensate for this. This is shown in Equation (2),

$$\eta = \eta_0/(1 - V/V_{max})^{2.5} \tag{2}$$

where η and η_0 are the apparent viscosity of the molten mixture and the viscosity of the molten metal without particles, respectively, and V and V_{max} are the volume fraction of particles and the maximum packing fraction, respectively [5]. As the equation shows, the apparent viscosity approaches infinity as the volume fraction of particles approaches the maximum packing fraction.

The introduction of hard ceramic particles into a metal matrix is an effective way to improve the wear performance of a material, but the corresponding reduction in toughness is often extremely substantial, even if the host matrix is an alloy that is specifically designed for excellent toughness [6]. The use of centrifugally-cast FGMMCs is a potential solution to this problem. For example, in high wear applications that require some degree of toughness, the FGMMC would ideally have a high volume fraction of ceramic particles on the exposed surface of the material for improved wear performance, but a low volume fraction of ceramic particles (or none) within the bulk material for toughness.

It is worth mentioning that the innermost periphery of centrifugal castings tend to contain unwanted (low density) inclusions [7] and porosity (from gas and shrinkage) [8], and therefore, the inward distribution of reinforcing particles is not optimal. However, if a wear resistant interior is desired (for instance, in pipes), this can nonetheless be achieved by using a reinforcing ceramic phase that is less dense than the molten metal as has been demonstrated in centrifugally cast TiC – Fe FGMMCs [9]. Since WC is one of the densest carbides [10], it is not surprising that WC has been explored as the reinforcing phase for a centrifugally-cast Hadfield steel FGMMC [11] where outward migration of WC particles resulted in a wear resistant outer surface layer. As this FGMMC suffered no loss in toughness in the interior, it displayed superior impact wear performance relative to an unreinforced Hadfield steel.

Here, this concept is applied to high chromium white cast irons, a class of wear resistant ferrous alloys [12-14], to create and characterise an FGMMC where the wear performance of the outer surface is further improved without compromising the already limited toughness of the cast iron alloy that makes up the bulk material. This was verified through hardness, sliding wear and three-point bending tests. NbC is selected as a potential reinforcing phase as NbC is not only harder than WC [10], but will not dissociate into individual Nb and C atoms in molten ferrous alloys, as is the case for WC [15]. Dissociation of the reinforcing carbide phase is highly undesirable as it significantly alters the composition of the host cast iron matrix, especially that of the C content. NbC additions, therefore, allow for a more precise control of the host alloy's composition and microstructure [16].

2. Material and Methods

There are several advantages in developing a centrifugally-cast *hypo-eutectic* high chromium white cast iron FGMMC for high wear applications. Firstly, high chromium white cast iron alloys naturally contain significant amounts of hard eutectic M_7C_3 carbides that result in excellent wear performance at the expense of impact toughness [12-14]. Therefore, any method to improve wear performance without an accompanying detriment to toughness is highly desired and a centrifugally cast FGMMC offers a potential solution. Secondly, since all M_7C_3 carbides will form through eutectic solidification, their distribution throughout the entire composite *should not be affected by centrifugal forces*, allowing us to circumvent one of the biggest limitations of using centrifugal forces to create a wear resistant outer surface: the maximum packing fraction of ceramic particles as governed by Stokes' law and Brinkman's equation. Thirdly, substantial work has already been undertaken on the use of carbide forming elements in this class of alloys to form various types of extremely hard carbide particles, such as TiC, WC, VC and NbC [13, 14, 17-22], that are harder than M_7C_3 carbides, in order to improve wear performance and/or to refine existing microstructures.

Since a high-quality wear-resistant surface layer is desired, the outward distribution of ceramic particles is preferred and therefore, the chosen ceramic phase should be denser than the molten high chromium white cast iron alloy used (as mentioned prior). NbC was confirmed to be a viable option using Thermo-Calc® since the density of the molten cast iron chosen for this study was predicted to be 6.63 g/cm^3 at its liquidus temperature (1310 ^{o}C) while the density of NbC was predicted to be 7.53 g/cm^3 at the same temperature. The proposed NbC - high chromium white cast iron FGMMC was centrifugally cast by Weir Minerals Australia Ltd., using the company's pending patent process [23]. The overall nominal chemical composition of the casting, designed to result in 15 vol% NbC particles through an *in-situ* reaction of Nb and C, is shown in Table 1. The resulting cylindrical casting has a diameter of 135 mm and a wall thickness of 28 mm, with a typical cross-section shown in Figure 1. All analyses were performed in the as-cast condition.

Table 1. Nominal composition of the centrifugally-cast NbC - high chromium white cast iron FGMMC.

Elements	Cr	Nb	C	Mn	Si	Cu	Mo	Ni	Fe
Wt%	23.8	13.3	3.1	1.1	1.3	1.3	0.9	1.7	53.5

Figure 1. Typical section of the centrifugally-cast high chromium white cast iron - NbC FGMMC. The approximate diameter and wall thickness of the casting are 135 mm and 28 mm respectively.

Material characterisation was done using optical microscopy (Zeiss Axio microscope with an accompanying AxioVision software), and scanning electron microscopy (Zeiss Ultra Field Emission Gun scanning electron microscope (SEM) and a Zeiss Evo Tungsten Filament SEM). The Zeiss Ultra is equipped with an energy dispersive X-ray spectroscopy (EDS) detector and an electron backscatter diffraction (EBSD) detector, which were both utilised simultaneously for phase characterisation (EBSD alone was unable to accurately distinguish between NbC and austenite due to the similarity in their crystal structures). The combined EDS and EBSD scans were analysed using Oxford Instrument's HKL Tango software. The sample preparation involved coarse grinding followed by fine polishing with diamond suspensions of 3 µm and 1 µm for most analyses while an additional polishing step involving OP-S colloidal silica suspension was used for EBSD.

The volume fraction and distribution of NbC particles and M_7C_3 carbides were determined by analysing low magnification, high resolution backscatter electron SEM images taken at 1 mm intervals along the radius of the casting using the Leica Application Suite: Phase and Grain Analyser. This software package enables the measurement of the volume fractions of both carbide phases and the NbC particle sizes through greyscale contrast. Vickers bulk-hardness tests (10 kg load, 15 s dwell time) were also conducted at approximately 1 mm intervals, radially across the casting in order to relate the distribution and volume fraction of NbC particles to bulk hardness values. Three indents were conducted per interval.

Finally, to relate the observed microstructure and bulk hardness values of the outer layer and the bulk material to their respective wear performance and fracture toughness, test samples of specific dimensions were extracted from the relevant regions using electric discharge machining. The wear plates had dimensions of 35 mm x 35 mm x 5 mm while the dimensions of the fracture toughness three-point bend notched specimens are shown in Figure 2. A fatigue pre-crack was introduced at the top of the notch of each three-point bend specimen prior to each test using an Instron 8501 Servo-Hydraulic machine by applying a cyclic load between 200 N and 2000 N at a frequency of 5 Hz. The fracture toughness tests were then conducted as outlined by ASTM E399 with a span of 64 mm [24], and three tests were performed per region analysed. The crack mouth opening displacement of the specimens was tracked using a digital image correlation technique on images captured with a Nikon D810 36.3 MP camera equipped with a 105 mm Micro lens at intervals of 4 s. Finally, the fracture path was also analysed using the SEMs. Due to the thickness of the NbC rich layer that will form on the outer layer of the casting (discussed subsequently), and to avoid three-point bend specimens that are too small, the three-point bend specimens were extracted such that the 16 mm widths (and therefore, the notch direction) were oriented along the tangent direction of the cylinder. While this may not reflect an inward crack propagation from the outer layer (i.e. normal direction to the cylinder), the relation between NbC volume fraction and distribution and the fracture toughness are still valid from a microstructural perspective.

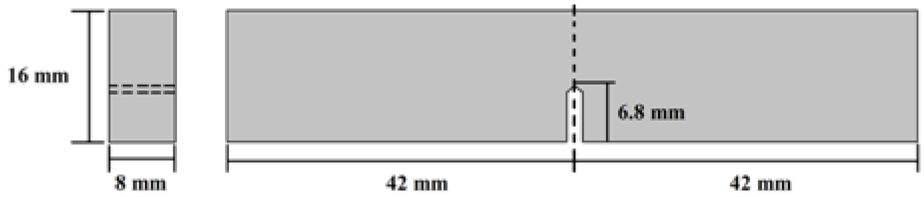

Figure 2. Schematic of the three-point bend specimens.

The relative wear performance was determined using dry sliding pin-on-disc wear tests on the extracted wear plates under ambient conditions against 3 mm diameter Si_3N_4 balls [12, 20, 25]. Each test was conducted three times per sample with a track diameter of 9.5 mm, a rotation speed of 60 RPM, a total test time of 1 hour, and an applied load of 10 N. The wear volume loss of the samples was approximated using four cross-sectional wear track profiles obtained orthogonally across one another using a 3D optical profilometer (AEP Technology's NanoMap-1000WLI), as recommended by ASTM G99 [26]. Using Equation X1.1 from the same standard, also shown in Equation (3), the wear volume loss of each ball was approximated using the diameter of the wear scar as measured using optical microscopy. The use of this equation is valid because the wear scars of the balls were planar and circular, and therefore, the wear volume losses can be approximated using this equation, which represents the volume of a sphere cap.

$$\text{Ball (pin) volume loss, mm}^3 \text{ (volume of a sphere cap)} = (\pi h / 6)(3d^2 / 4 + h^2) \qquad (3)$$

3. Results and Discussion

3.1 NbC Particle Distribution

The general microstructure evolution across the FGMMC can be observed in the optical microscope images in Figure 3. In Figures 3a – c, large volume fractions of primary spherical NbC particles (dark grey) can be observed up to 8 mm from the outer periphery, which we shall hereinafter refer to as the *hard layer*. Between 8 and 9.5 mm (Figures 3d and e), there is an abrupt transition in microstructure and a sharp decrease in the number of primary NbC particles and the NbC volume fraction, though any primary NbC particle found here tends to be significantly coarser and dendritic (with spans exceeding 100 μm). Therefore, we shall hereinafter refer to this region as the *transition region*. NbC with a morphology resembling a eutectic phase, commonly referred to in the literature as *Chinese-*

script [13, 27-29], can also be observed here. Finally, the rest of the casting (Figures 2f – h), constitutes the *bulk material*, where Chinese-script NbC is predominantly observed and primary NbC particles are rare. Towards the innermost periphery, porosity can be observed (Figure 3h).

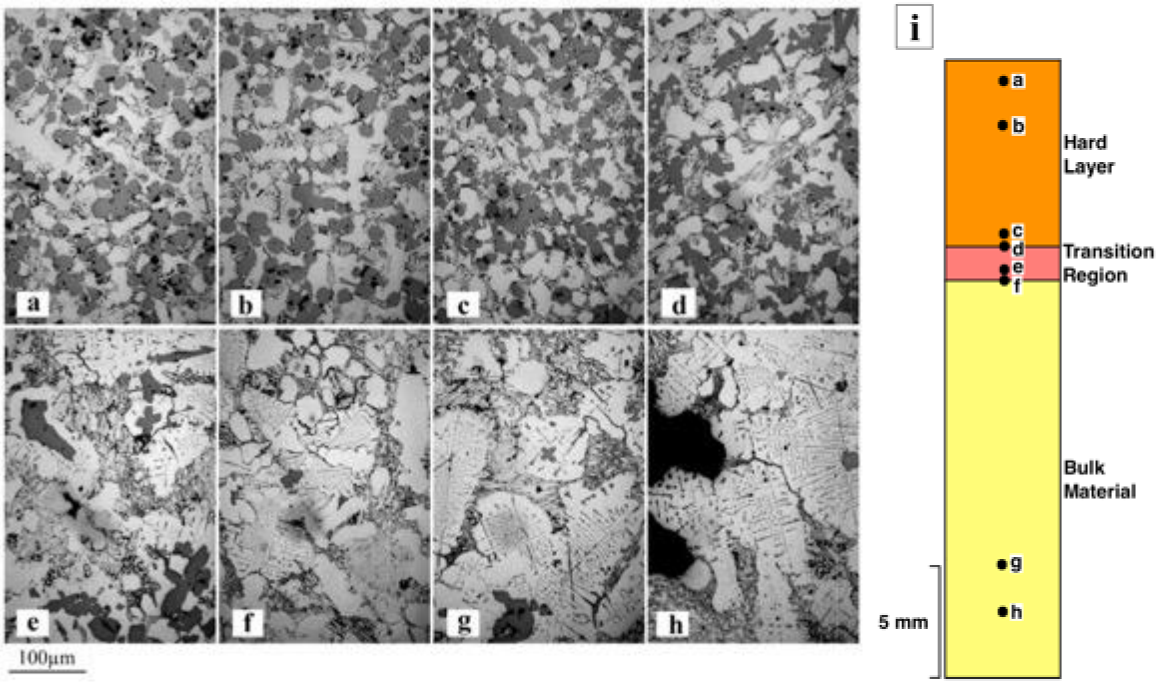

Figure 3. Microstructure of the casting with NbC particles (dark grey)– Distance from outer periphery: (a) 1mm, (b) 3 mm, (c) 8 mm, (d) 8.5 mm, (e) 9.5 mm, (f) 10 mm, (g) 23 mm, (h) 25 mm, (i) schematic showing where the micrographs (a) – (h) were obtained from the casting.

The effect of primary NbC particle size on its distribution with respect to distance from the surface is shown in Figure 4. For simplicity, only spherical NbC particles will be considered for this analysis and thus, the figure only shows NbC particle distribution in the hard layer (up to 8 mm from the outer periphery). As shown in the figure, there is a greater tendency for a spherical NbC particle with a larger diameter to end up at the outer periphery of the hard layer. Of all NbC particles that exceed 40 µm in diameter, approximately 35 % of them ended up within 1 mm of the outer periphery while only 4 % of these particles are 8 mm away from the outer periphery. Similarly, there is a significantly higher fraction of fine NbC particles (< 10 µm in diameter) at 8 mm as opposed to 1 mm from the outer periphery, at approximately 19 % and 9 %, respectively. This distribution is in good agreement with Stokes' Law (Equation (1)) in that primary NbC particles, which are denser than the molten metal, ended up at the outer periphery of the casting, with the larger particles tending to end up further outward. Since a dendritic primary NbC particle experiences more drag than a spherical one, extremely coarse dendritic primary NbC particles tend to end up at the transition region just beyond the hard layer.

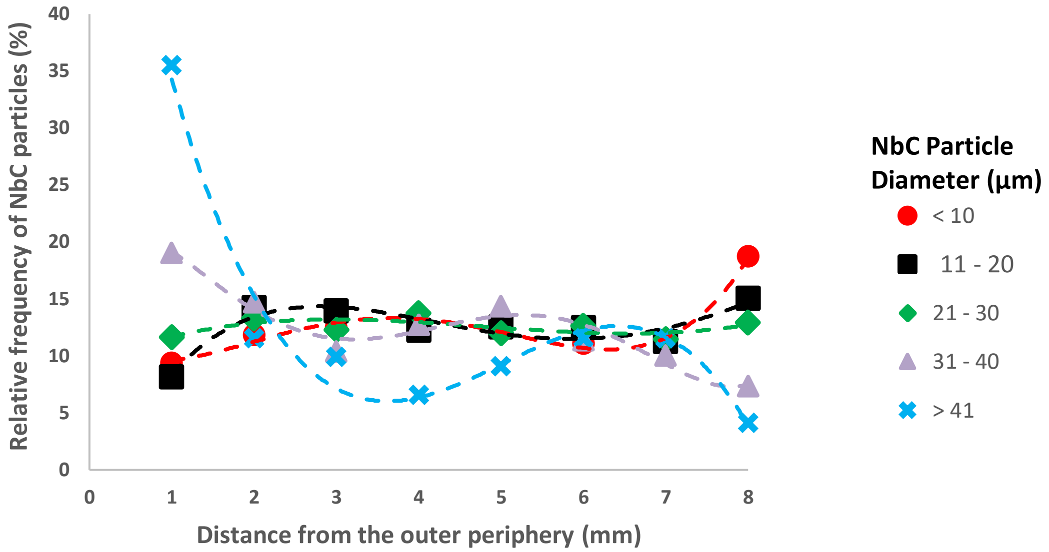

Figure 4. Particle size distribution of primary NbC particles at the hard layer measured at 1 mm intervals from the outer periphery. As an example, of all NbC particles with diameter > 41 µm, as shown with blue crosses, 35 % of them ended up at 1 mm from the outer periphery while 4 % of them ended up at 8 mm from the outer periphery.

The overall volume fraction of NbC measured at 1 mm intervals, up to 20 mm from the outer periphery, across the radius of the entire casting is shown in Figure 5. The maximum packing fraction of NbC particles at the outermost periphery is 30 vol%. This then decreases radially inward to approximately 25 vol% at the end of the hard layer. This means that, for the casting parameters used (such as the centrifuge spinning rate, the duration of centrifugal spinning, and the cooling rate), the effective viscosity at the outermost periphery reaches a maximum when the NbC volume fraction reaches 30 vol% (as described for Equation (2)) which then prevents further migration of NbC particles to the region. Achieving such a high volume fraction of primary ceramic particles in conventional ferrous MMCs through melting and casting processes is extremely difficult [30], so this demonstrates the advantage of centrifugal casting in fabricating wear resistant materials. From the outermost periphery, the packing fraction then decreases linearly across the material up to the inner edge of the hard layer at 8 mm. At the transition region, Figure 5 shows a substantial drop in NbC volume fraction 8-10 mm from the outer edge. The bulk material consists of approximately 6 vol% eutectic Chinese-script NbC that is not affected by centrifugal forces.

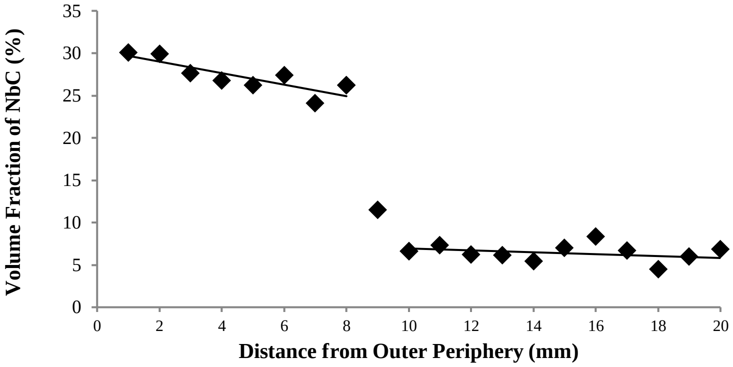

Figure 5. Distribution of NbC by volume fraction at 1 mm intervals from the outer periphery.

3.2 General microstructure

The solidification path of the casting, based on the composition in Table 1, as predicted by Thermo-Calc®, is shown in Figure 6. As expected, the overall final NbC volume fraction is 15 vol%. However, at the liquidus temperature of 1310 ^{o}C (where δ - ferrite starts to form), approximately 3 vol% of this NbC is still in solution within the liquid. Between 1310 ^{o}C and 1270 ^{o}C, the remaining 3 vol% NbC forms simultaneously with δ - ferrite. While this resembles a eutectic reaction, the wide temperature range means that it could be argued that it would be more accurate to refer to it as a "pseudo-eutectic" reaction [16]. However, to be consistent with the established literature, we shall still refer to it as a eutectic reaction [13, 27-29]. As the casting cools through this eutectic temperature range (approximately 1290 - 1280 ^{o}C), the eutectic M_7C_3 and austenite phase also form. This could imply that there are two separate eutectic systems occurring within this narrow temperature range, the M_7C_3 and austenite reaction, and the NbC and δ - ferrite reaction. As the casting continues to cool down, under equilibrium conditions, the δ - ferrite is expected to fully transform into austenite while the M_7C_3 carbides are expected to transform into $M_{23}C_6$ carbides. However, due to the relatively fast cooling rate and the consequent non-equilibrium nature of the casting, the actual phases and their respective volume fractions are expected to differ from Thermo-Calc® predictions.

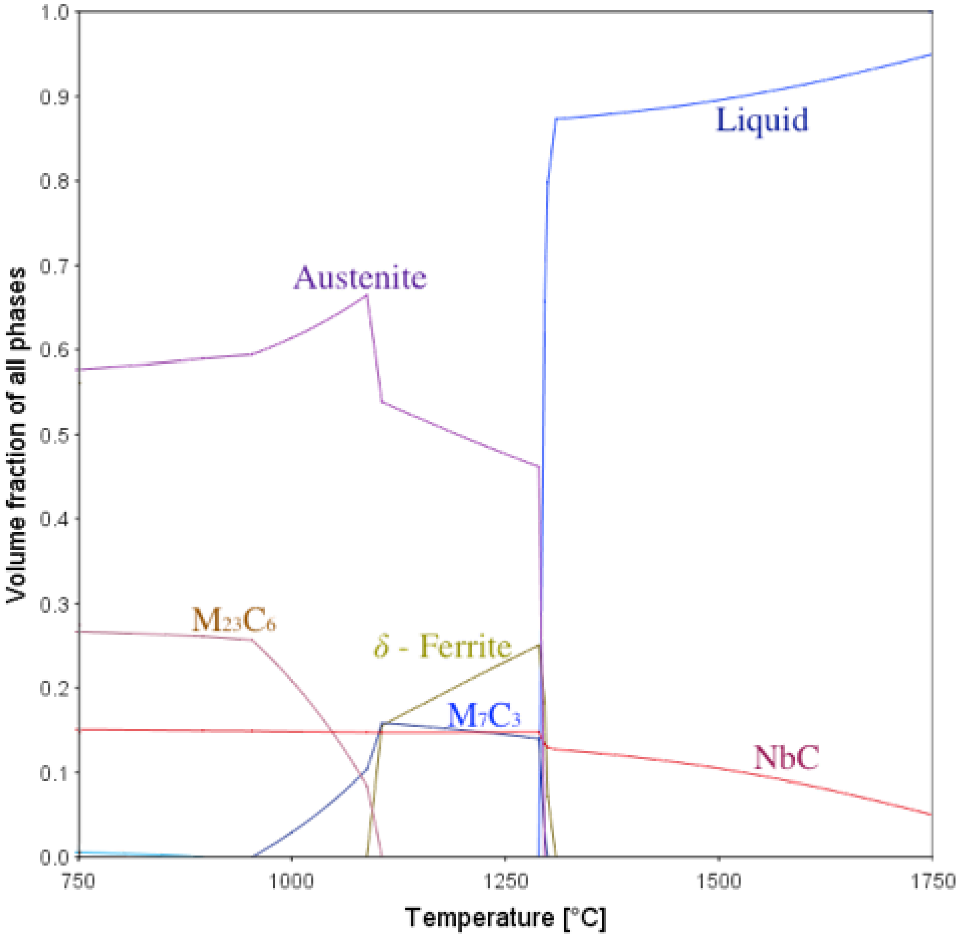

Figure 6. Thermo-Calc® predictions of the solidification process of the centrifugally-cast NbC - high chromium white cast iron FGMMC.

The microstructures of the hard layer and the transition region are shown in Figures 7 and 8, respectively, where NbC, M_7C_3, austenite and martensite can be observed. Centrifugal forces would be expected to drive most (if not all) primary NbC particles formed in the molten metal prior to the liquidus temperature to the hard layer. As shown previously in Figure 3, the transition region marks the drastic change in NbC morphology from the hard layer to the bulk material, and therefore, both primary and Chinese-script NbC can be observed, as shown in Figure 8a. The primary austenite dendrites observed in both Figures 7 and 8 were most likely formed as δ - ferrite (as shown in Figure 6) but were transformed into austenite upon cooling. The retention of austenite at room temperature is typical of *as-cast* high chromium white cast iron alloys, since the rapid cooling rate causes austenite to be supersaturated with Cr and C, which suppresses the martensite start temperature (M_s) to below room temperature, preventing the formation of martensite [31]. However, the eutectic formation of M_7C_3 carbides will deplete surrounding austenite regions of Cr and C, thus causing a localised increase in the austenite M_s to above room temperature [31, 32]. Therefore, the austenite *surrounding* the M_7C_3 carbides transformed into martensite upon cooling, as can be seen in Figures 7b and 8b. The M_7C_3 carbide volume fraction in the hard layer and the transition region were measured to be approximately 12 vol% and 14 vol% respectively. Interestingly, the M_7C_3 structure in the hard layer is significantly more refined, which could be due to the presence of a high volume fraction of primary NbC particles restricting the M_7C_3 solidification front during the eutectic reaction.

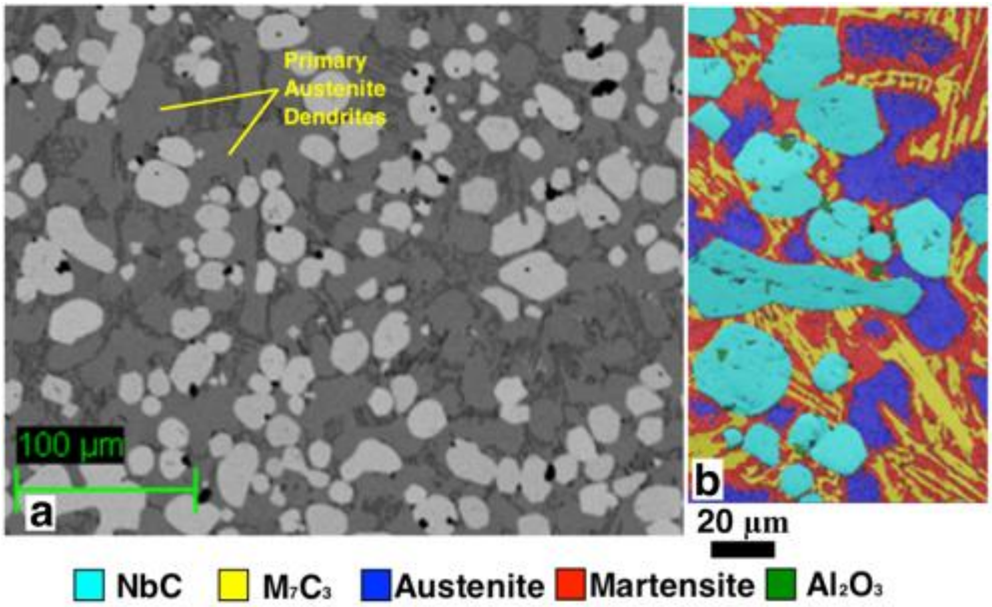

Figure 7. (a) Backscatter electron image showing the microstructure of the hard surface layer, with NbC shown in light grey, ferrous matrix shown in mid grey, M_7C_3 in dark grey, and (b) EBSD phase map revealing the phases present.

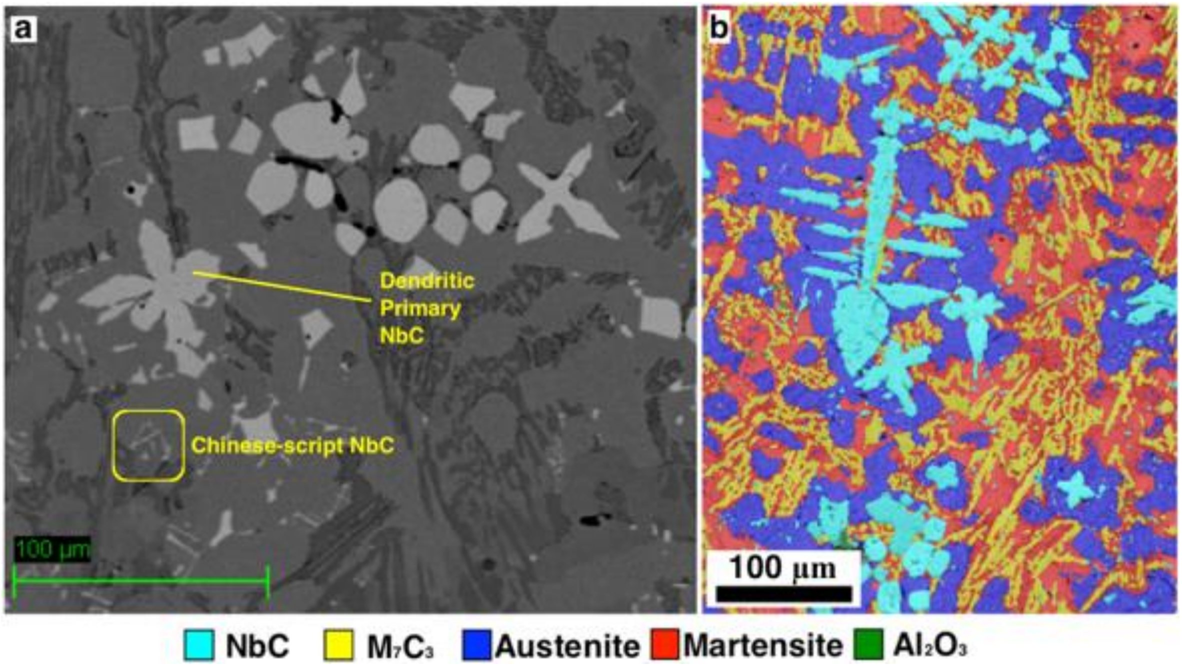

Figure 8. (a) Backscatter electron image showing the microstructure of the transition region, with NbC shown in light grey, ferrous matrix shown in grey, M_7C_3 in dark grey, and (b) EBSD phase map revealing the phases present.

The general microstructure of the bulk material is shown in Figure 9. Interestingly, the eutectic Chinese-script NbC and the eutectic M_7C_3 form independent eutectic clusters that are not interconnected. This is consistent with the Thermo-Calc® results mentioned earlier where two separate binary eutectic systems were predicted, with the NbC and δ - ferrite system forming slightly earlier than the M_7C_3 and austenite system. The subsequent transformation of δ - ferrite to austenite then results in a microstructure where the Chinese-script NbC appear to be embedded *within* primary austenite dendrite arms. Similarly, as the M_7C_3 carbides are located *between* the austenite dendrite arms, this confirms that the eutectic M_7C_3 was formed later than the eutectic Chinese-script NbC. This solidification sequence can be summarised as follows with superscripts 1 and 2 differentiating the two austenite phases with different chemical compositions: L ⇒ NbC + δ - ferrite (first eutectic reaction), L ⇒ M_7C_3 + austenite^1 (second eutectic reaction), δ - ferrite ⇒ austenite^2, austenite^1 ⇒ martensite. The M_7C_3 volume fraction in the bulk material was also found to be approximately 14 vol%.

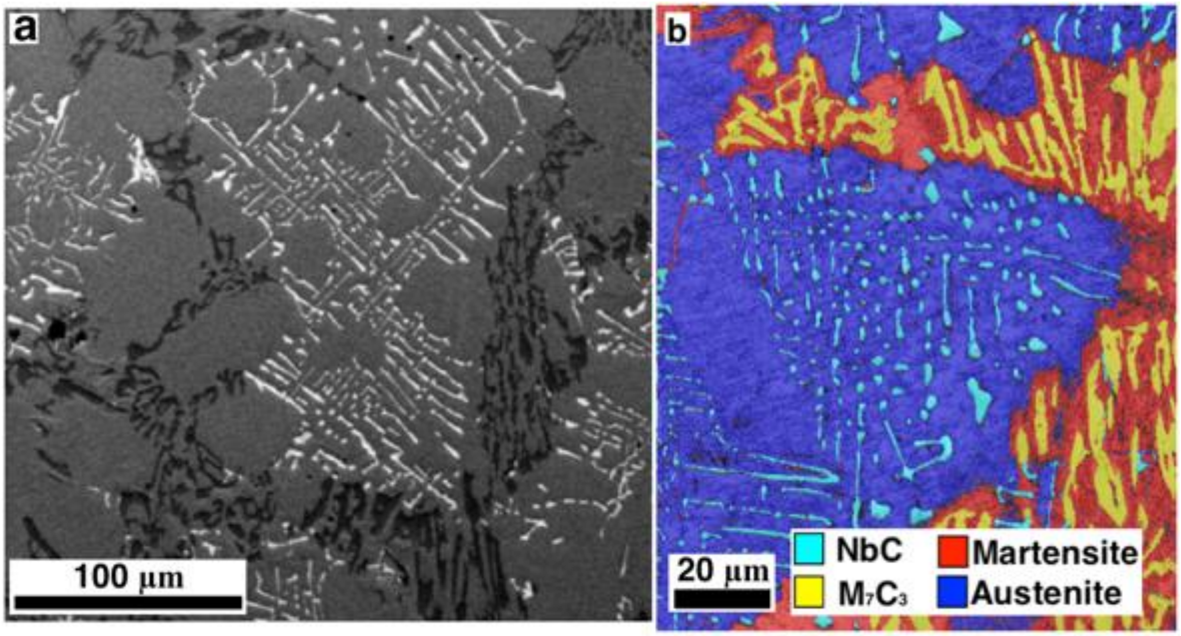

Figure 9. (a) Backscatter electron image showing a cluster of Chinese-script NbC (light grey) within an austenite grain (mid grey) in the bulk material surrounded by eutectic M_7C_3 carbides (dark grey) and (b) EBSD phase map revealing the phases present in this region.

The presence of Chinese-script NbC confirms that some NbC remains dissolved in the molten white cast iron during solidification, and the distribution of the dissolved Nb and C atoms is not expected to be affected by centrifugal forces (which is why Chinese-script NbC was found throughout the bulk material). Therefore, it is interesting that Chinese-script NbC was not observed in the hard layer. This contrasts with the results obtained by Kesri and Durrand-Charre who found eutectic NbC in all of the Fe-Cr-Nb-C alloys they investigated, regardless of whether primary NbC formed [27]. In our own previous work on AISI 440 martensitic stainless steels reinforced with NbC, we found that during the eutectic NbC reaction, dissolved Nb and C atoms in the molten metal would often diffuse towards an existing primary NbC particle (if there is one in proximity) in order to nucleate off the primary particle, usually resulting in the primary particle being surrounded by Chinese-script NbC that all share the same crystal orientation [16]. However, when the volume fraction of NbC particles was sufficiently high (> 20 vol% primary NbC), there will be plenty of primary NbC particles in close proximity (short diffusion path) to the dissolved Nb and C atoms, allowing the atoms to simply react and nucleate off the nearest primary NbC particle, thus coarsening it instead of forming elaborate Chinese-script structures. A similar phenomenon could explain why Chinese-script

NbC was not observed in the hard layer in this case, where the volume fraction of primary NbC particles was between 25 and 30 vol%.

3.3 Bulk Hardness

The macro-hardness results obtained radially at 1 mm intervals across the casting are shown in Figure 10. There is an approximately linear decrease in bulk hardness from approximately 525 HV to approximately 460 HV across the hard layer (1 to 8 mm from the outer periphery). This result is consistent with the decrease in NbC volume fraction shown in Figure 5. At the transition region (8 to 10 mm), there was an accompanying sharp decline in hardness to approximately 380 HV as the volume fraction of NbC fell from 25 vol% to approximately 7 vol%. The rest of the material featured an average hardness of approximately 364 HV. Of course, the bulk hardness of the casting is also affected by the volume fraction of M_7C_3 carbides, which is slightly lower in the hard layer. The average hardness values and carbide volume fractions for the hard layer and the bulk material are summarised in Table 2, with the hard layer containing a total of almost twice the volume fraction of carbides as compared to the bulk material.

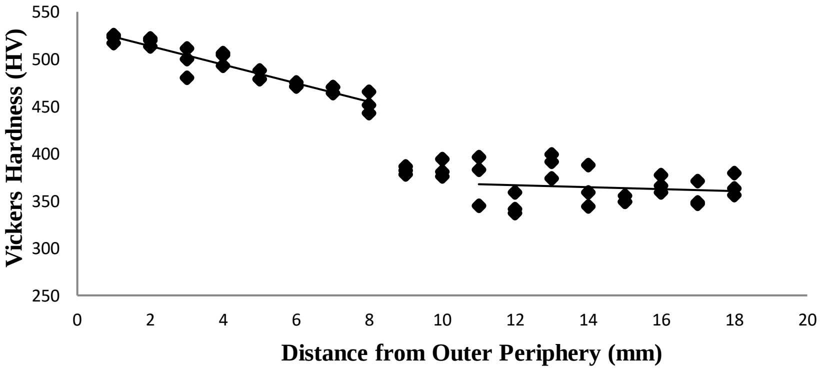

Figure 10: Vickers bulk hardness test results of the casting taken at 1 mm intervals from the outer periphery. Three indents were done at each interval as shown in the figure.

Table 2. The average volume fraction of the carbide phases and the resulting average hardness values of the hard layer and the bulk material.

	NbC Vol%	M_7C_3 Vol%	Total Carbide Vol%	Bulk Hardness (HV)
Hard Layer	27	12	39	489
Bulk Material	6	14	20	364

3.3 Dry Sliding Wear

The results of the dry sliding wear tests conducted with Si_3N_4 balls are shown in Figure 11. The larger standard deviation of the hard layer can be explained by the variations in primary NbC volume fraction across the flat wear plate (i.e. the edges of the wear plate contain more primary NbC particles by virtue of being closer to the outermost periphery of the cylindrical casting). Conversely, the small standard deviation of the bulk material is consistent with the fact that NbC volume fraction was essentially unchanged throughout this region. Regardless, what is important is that the hard layer experienced approximately half the wear loss of the bulk material, proving that centrifugally casting an FGMMC that is wear resistant on the outer layer is viable. This is because the hard layer contains almost twice the volume fraction of carbides (on average) than the bulk material which then allows it to function better as a wear resistant material. The increased hardness of the hard layer also resulted in an increase in the wear rate of the Si_3N_4 balls.

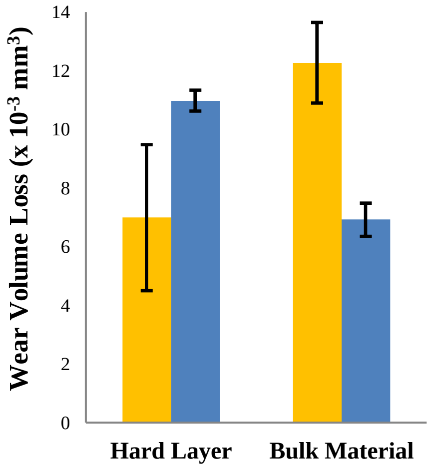

Figure 11. Sliding wear volume loss results of both the high chromium white cast iron FGMMC (yellow) and the Si_3N_4 balls (blue). The results are an average of three tests with the error bars showing the corresponding standard deviation.

SEM images of the wear tracks are shown in Figure 12. The dominant wear mechanism experienced by both the hard layer and the bulk material is micro-fracture. Some oxide was also observed on the wear tracks of both regions. Since this sliding wear test was conducted under ambient conditions, the oxide debris is most likely hydrated silica due to a tribo-chemical reaction experienced by the Si_3N_4 balls in the presence of humidity [33, 34]. While the hard layer and the bulk material both experience material wear losses through micro-fracturing, the degree of material loss is best represented by the 3D images of the wear tracks obtained using the optical 3D profilometer, as shown in

Figure 13. These images show that the typical wear track of the bulk material is substantially wider and deeper than that of the hard layer.

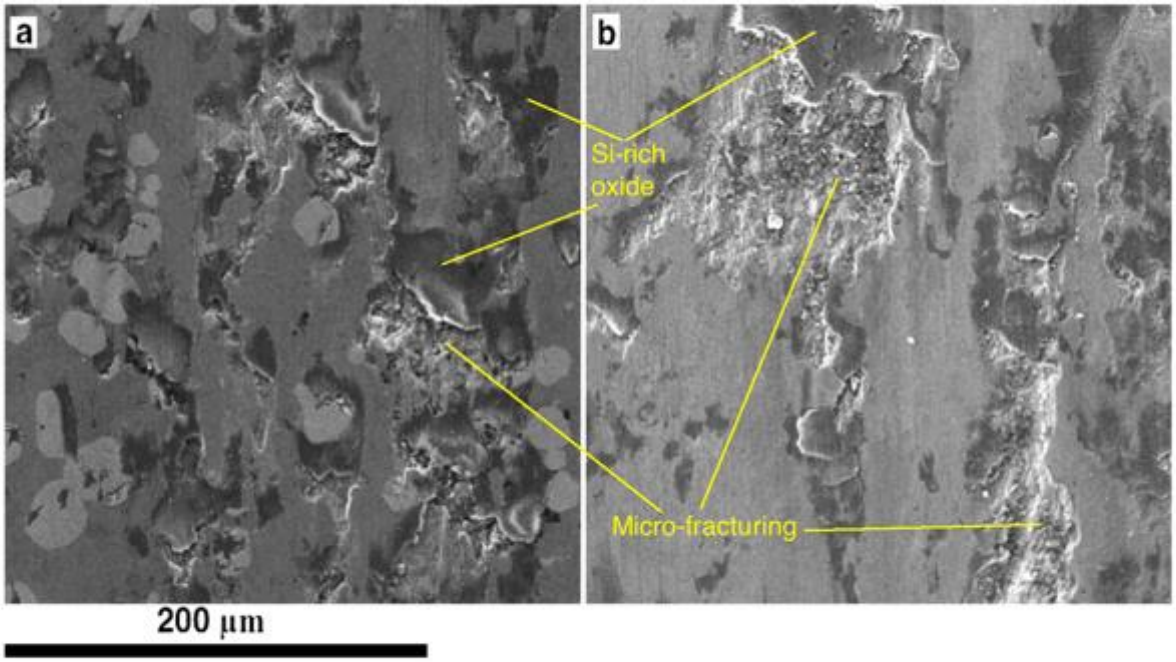

Figure 12. Backscatter electron images of the wear track of the (a) hard layer and (b) the bulk material. The oxide debris is shown by the dark color in the images.

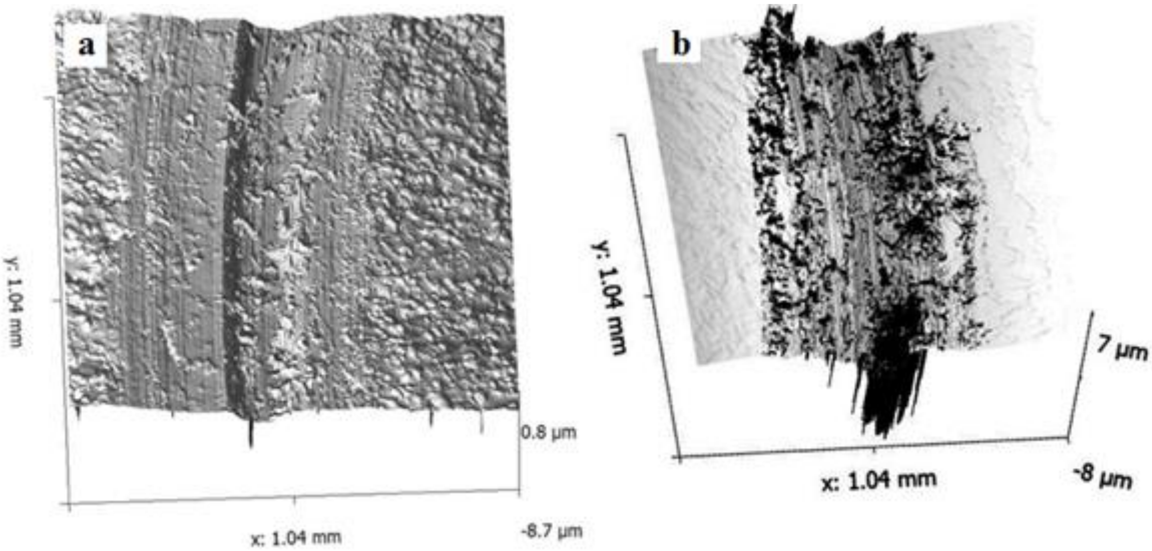

Figure 13. Typical 3D profile of the wear track of the (a) hard layer and the (b) bulk material.

3.4 Fracture Toughness

Due to the thickness of the three-point bend specimens (8 mm, as shown in Figure 2) and the fact that the casting is cylindrical, it was unavoidable that the three-point bend specimens from the hard layer also capture the transition region (approximately 1 mm overlap). However, for simplicity, we shall simply relate the obtained fracture toughness results of the hard layer to the average carbide volume fractions reported in Table 2. The fracture toughness results (K_{Ic}) obtained from the three-point bending tests for the hard layer and the bulk material are 20.8 ± 0.54 MPa$\sqrt{m}$ and 26.7 ± 1.09 MPa$\sqrt{m}$ respectively. It should be noted here that the P_{max}/P_Q (where P_{max} and P_Q represent the maximum load and the yield load during three-point bending) linear-elastic validity check outlined in ASTM E399 was found to be approximately 1.13 for the bulk material [24]. Since the validity requirement for computing linear-elastic fracture toughness by three-point bending is 1.10 (an exceedance indicates that failure is not purely linear-elastic), the exceedance of this value by the bulk material is very marginal, and for comparative purposes, we shall assume that all deformation of the bulk material was linear elastic. Therefore, the results demonstrate that this FGMMC fabricated by centrifugal casting not only has a harder, more wear resistant, outer layer, but that the bulk material is significantly tougher. In order to put these toughness values in the context of high chromium white cast irons, we refer to the relationship between M_7C_3 volume fraction and fracture toughness (K_{Ic}) in high chromium white cast irons that was developed by Zum Gahr and Scholz [35]. The bulk material and the hard layer, which contain a combined NbC and M_7C_3 volume fraction of 20 vol% and 39 vol% respectively, is comparable to the fracture toughness of conventional *austenitic* high chromium white cast iron alloys containing the same M_7C_3 volume fractions. This is illustrated in Figure 14.

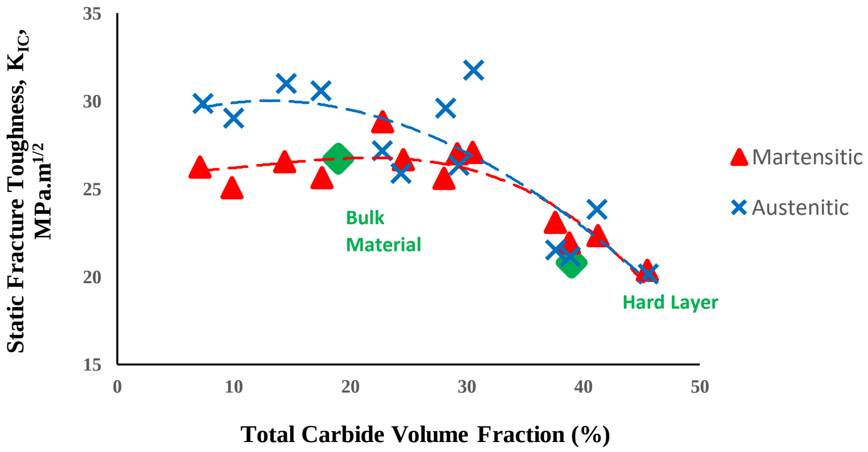

Figure 14. The toughness of the hard layer and the bulk material (both represented by green diamonds) as a function of carbide volume fraction relative to conventional martensitic (red triangles) and austenitic (blue crosses) high chromium white cast iron alloys as reported by Zum Gahr and Scholz [35].

As shown in Figure 14, the hard layer performed within an expected range. Interestingly, at such a high volume fraction of carbides, the fracture toughness is expected to be unchanged, whether the matrix is austenitic or martensitic. This means that, after a hardening heat treatment, the hard layer should experience a further improvement in wear performance with little compromise to its toughness. At first glance, the bulk material, while tougher, seemed to have performed more poorly than expected for an austenitic high chromium white cast iron containing 19 vol% carbides. However, it is also worth noting that the toughness of austenitic high chromium white cast irons also shows a considerable amount of scatter, as can be seen by the distribution of blue data points in the figure. Once this is taken into consideration, the bulk material, while showing a lacklustre fracture toughness, nevertheless did perform within an expected range.

In order to understand the toughness results, backscatter electron images of the fracture surfaces were obtained and are shown in Figure 15. Figures 15a and c are the plan and sectional views of the fracture surface of the hard layer, respectively. As can be seen, crack propagation in the hard layer often occurs preferentially *through* the NbC particles. The extensive amount of primary NbC fracturing along the crack path and an absence of delamination of NbC from the ferrous matrix indicates that the bond strength is sufficiently strong for loads to be effectively transferred between the two phases. Since the M_7C_3 carbide networks are considerably finer than the primary NbC particles in the hard layer, it is easier for the fracture path to travel across the NbC particles than to pass through networks of alternating layers of M_7C_3 and austenite. Since the fracture path mostly propagates through the NbC particles and the M_7C_3 network as opposed to through the austenite phase, transforming the ferrous matrix into martensite should have little implications to fracture toughness, as was mentioned previously. While the toughness of the hard layer fell within an expected range, improvements to fracture toughness should potentially be achievable by using ceramic phase that is tougher than NbC (as well as denser than the molten metal) or by refining the NbC particle size.

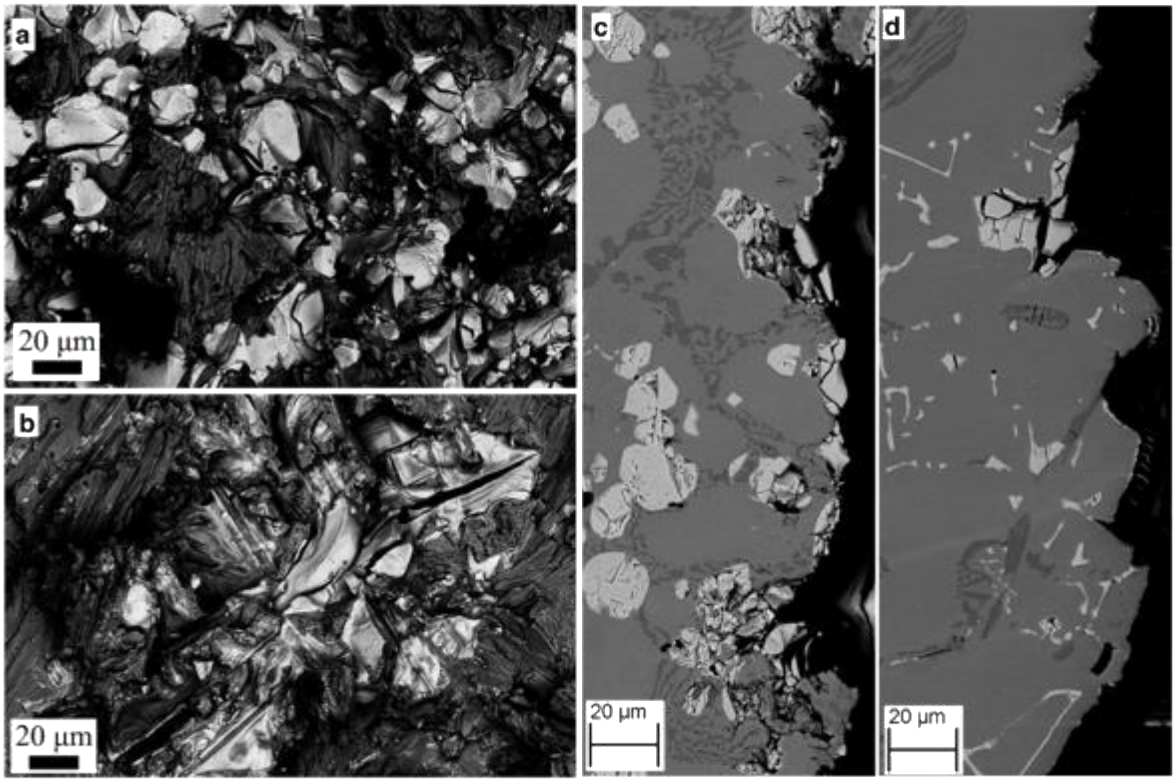

Figure 15. Backscatter electron images showing the plan view of the fracture surface of the (a) hard layer and the (b) bulk material, and the section view of the (c) hard layer and the (d) bulk material.

Figures 15b and d are plan and sectional views of the crack propagation path in the bulk material respectively. Both figures show that the fracture path preferentially propagates *across entire Chinese-script NbC arms*. While the Chinese-script NbC is extremely thin, the arms can span up to and beyond 100 μm wide (for an example, refer to Figure 9a). Since the crack travels along these arms, having a wide network of Chinese-script NbC facilitates an easy propagation. This results in a highly planar and angular fracture path as can be seen in Figure 15d, with entire cleaved Chinese-script NbC arms exposed along the fracture surface, as seen in Figure 15b. While the M_7C_3 networks are coarser than the Chinese-script NbC networks, the varying orientations of the M_7C_3 are unfavourable for crack propagation relative to the straight and highly angular Chinese-script NbC. Even though the bulk material was tougher than the hard layer, the sub-optimal toughness in the bulk material was due to the presence of Chinese-script NbC. Thus, the composition of the matrix material should be chosen to minimise the NbC solubility at liquidus in order to prevent the formation of Chinese-script NbC structures, or ways to refine these structures should be explored.

Alternatively, a cast-decant-cast (CDC) approach could also be potentially used in conjunction with centrifugal casting to not only solve the Chinese-script NbC problem, but also to create a significantly tougher bulk material. Conventionally, the CDC approach [36] is typically used to create a functionally-graded material using two different alloys by pouring the melt of the first alloy into a mould. Since this alloy would first solidify inwardly from the mould wall, once a desired thickness of this alloy has solidified, the excess molten metal can be poured away. Then, the melt of the second alloy can be poured on top of the first alloy, with the temperature of the second alloy sufficiently high to partially melt the first alloy at the region of contact. Upon solidification, a functionally-graded material between the two alloys can be achieved. Therefore, if the proposed NbC – high chromium white cast iron was centrifugally cast but only the hard layer was allowed to solidify inwardly from the cylindrical mould wall, the excess molten metal that contains dissolved NbC can be poured away. The melt of a second alloy, preferably a steel since steels are tougher and have a higher liquidus temperature (to partially melt the NbC – high chromium white cast iron layer at the region of contact), can then be poured into the spinning mould. Upon solidification, this FGMMC would then contain a very hard and wear resistant surface (a high chromium white cast iron reinforced with 30 vol% NbC particles) and an extremely tough bulk material (a steel).

4. Conclusion

Centrifugal casting has been shown to be a viable option for producing high quality castings of functionally-graded NbC – high chromium white cast iron composites with a harder, more wear resistant surface layer and a softer, tougher core through the outward distribution of primary NbC particles as a result of centrifugal forces. Primary NbC migration was also found to be consistent with Stokes’ law, with larger NbC particles having a greater tendency to migrate further outward during casting. With the nominal composition of the FGMMC designed to form approximately 15 vol% NbC and casting dimensions of a diameter of 135 mm and a wall thickness of 28 mm, the casting process resulted in a hard NbC-rich hard layer at the outer periphery that measured 8 mm thick, followed by a 1.5 mm thick transition region and the softer bulk material. The bulk material largely contained approximately 6 vol% eutectic Chinese-script NbC.

Across the 8 mm thick hard layer, from the outermost periphery, there was a relatively linear downward gradient in the NbC volume fraction, from 30 vol% to 25 vol% NbC. This corresponds to the maximum packing fraction of

NbC particles for the casting parameters used. Such volume fractions are difficult to accomplish with traditional casting methods. If more NbC was added to the melt, the thickness of the hard layer would be expected to increase with the same decreasing linear gradient of NbC volume fraction. To circumvent the problem of the maximum packing fraction, a hypo-eutectic high chromium white cast iron was used as the matrix material in order to utilise eutectic M_7C_3 carbides to further augment the volume fraction of ceramic phases at the hard layer. This is effective because these eutectic M_7C_3 carbides form only after the ferrous matrix has started solidifying and therefore, are not affected by centrifugal forces. This, however, also means that the bulk material contains some M_7C_3 carbides which would decrease its toughness.

The bond strength between NbC and the ferrous matrix was strong enough such that carbide-matrix delamination did not occur during three-point bending fracture toughness tests. However, while the bulk material was tougher than the hard layer, its toughness was found to be sub-optimal when compared to traditional high chromium white cast irons of similar carbide volume fractions. This was attributed to the presence of Chinese-script NbC and therefore, designing alloys that reduces Chinese-script NbC and promote the formation of primary NbC particles is highly desirable. Alternatively, a cast-decant-cast approach to centrifugal casting may also be used to solve this problem.

Acknowledgements

Funding: This work was supported by Weir Minerals Australia Ltd.; the Australian government's Australian Postgraduate Awards scheme; the Australian Research Council [grant number: LP130100111 and Discovery Early Career Researcher Award: DE150101703]; the FEDER [grant number: POCI-01-0145-FEDER-007633]; and the facilities and assistance by the Australian Microscopy & Microanalysis Research Facility at the Australian Centre of Microscopy and Microanalysis, University of Sydney.

References

[1] Y. Watanabe, N. Yamanaka, Y. Fukui, Control of composition gradient in a metal-ceramic functionally graded material manufactured by the centrifugal method, Composites Part A: Applied Science and Manufacturing, 29 (1998) 595-601.
[2] Y. Watanabe, A. Kawamoto, K. Matsuda, Particle size distributions in functionally graded materials fabricated by the centrifugal solid-particle method, Composites Science and Technology, 62 (2002) 881-888.

[3] T.P.D. Rajan, R.M. Pillai, B.C. Pai, Characterization of centrifugal cast functionally graded aluminum-silicon carbide metal matrix composites, Materials Characterization, 61 (2010) 923-928.

[4] T. Ogawa, Y. Watanabe, H. Sato, I.-S. Kim, Y. Fukui, Theoretical study on fabrication of functionally graded material with density gradient by a centrifugal solid-particle method, Composites Part A: Applied Science and Manufacturing, 37 (2006) 2194-2200.

[5] H. Brinkman, The viscosity of concentrated suspensions and solutions, The Journal of Chemical Physics, 20 (1952) 571-571.

[6] E. Moghaddam, N. Karimzadeh, N. Varahram, P. Davami, Impact–abrasion wear characteristics of in-situ VC-reinforced austenitic steel matrix composite, Materials Science and Engineering: A, 585 (2013) 422-429.

[7] B. Lewis, Centrifugal casting, U.S. Patent 1831310, 1931.

[8] T. Rajan, R. Pillai, B. Pai, Centrifugal casting of functionally graded aluminium matrix composite components, International Journal of Cast Metals Research, 21 (2008) 214-218.

[9] M.R. Rahimipour, M. Sobhani, Evaluation of centrifugal casting process parameters for in situ fabricated functionally gradient Fe-TiC composite, Metallurgical and Materials Transactions B, 44 (2013) 1120-1123.

[10] R.J. Brook, Concise encyclopedia of advanced ceramic materials, Elsevier, 2012.

[11] G.-S. Zhang, J.-D. Xing, Y.-M. Gao, Impact wear resistance of WC/Hadfield steel composite and its interfacial characteristics, Wear, 260 (2006) 728-734.

[12] R.J. Chung, X. Tang, D.Y. Li, B. Hinckley, K. Dolman, Microstructure refinement of hypereutectic high Cr cast irons using hard carbide-forming elements for improved wear resistance, Wear, 301 (2013) 695-706.

[13] M. Filipovic, Z. Kamberovic, M. Korac, M. Gavrilovski, Microstructure and mechanical properties of Fe–Cr–C–Nb white cast irons, Materials & Design, 47 (2013) 41-48.

[14] X. Zhi, J. Xing, H. Fu, B. Xiao, Effect of niobium on the as-cast microstructure of hypereutectic high chromium cast iron, Materials Letters, 62 (2008) 857-860.

[15] A. Rokanopoulou, P. Skarvelis, G. Papadimitriou, Microstructure and wear properties of the surface of 2205 duplex stainless steel reinforced with Al 2 O 3 particles by the plasma transferred arc technique, Surface and Coatings Technology, 254 (2014) 376-381.

[16] W.H. Kan, Z.J. Ye, Y. Zhu, V.K. Bhatia, K. Dolman, T. Lucey, X. Tang, G. Proust, J. Cairney, Fabrication and characterization of microstructure of stainless steel matrix composites containing up to 25vol% NbC, Materials Characterization, 119 (2016) 65-74.

[17] M. Fiset, K. Peev, M. Radulovic, The influence of niobium on fracture toughness and abrasion resistance in high-chromium white cast irons, Journal of Materials Science Letters, 12 (1993) 615-617.

[18] C. He-Xing, C. Zhe-Chuan, L. Jin-Cai, L. Huai-Tao, Effect of niobium on wear resistance of 15% Cr white cast iron, Wear, 166 (1993) 197-201.

[19] M. Filipovic, Z. Kamberovic, M. Korac, B. Jordovic, Effect of Niobium and Vanadium Additions on the As-Cast Microstructure and Properties of Hypoeutectic Fe–Cr–C Alloy, ISIJ international, 53 (2013) 2160-2166.

[20] R.J. Chung, X. Tang, D.Y. Li, B. Hinckley, K. Dolman, Effects of titanium addition on microstructure and wear resistance of hypereutectic high chromium cast iron Fe–25wt.%Cr–4wt.%C, Wear, 267 (2009) 356-361.

[21] S. Mousavi Anijdan, A. Bahrami, N. Varahram, P. Davami, Effects of tungsten on erosion–corrosion behavior of high chromium white cast iron, Materials Science and Engineering: A, 454 (2007) 623-628.

[22] M. Filipovic, Z. Kamberovic, M. Korac, Solidification of high chromium white cast iron alloyed with vanadium, Materials transactions, 52 (2011) 386-390.

[23] X. Tang, K.F. Dolman, Composite Metal Product, US20170022588 A1 (Patent), (2014).

[24] ASTM, E399 - 12e3, Standard Test Method for Linear-Elastic Plane-Strain Fracture Toughness KIc of Metallic Materials, (2012).

[25] Y.P. Wang, D.Y. Li, L. Parent, H. Tian, Improving the wear resistance of white cast iron using a new concept – High-entropy microstructure, Wear, 271 (2011) 1623-1628.

[26] ASTM, G99 - 17, Standard Test Method for Wear Testing with a Pin-on-Disk Apparatus, (2017).

[27] R. Kesri, M. Durand-Charre, Phase equilibria, solidification and solid-state transformations of white cast irons containing niobium, Journal of materials science, 22 (1987) 2959-2964.

[28] F. Haddad, S. Amara, R. Kesri, S. Hamar-Thibault, Contribution to the study of the Fe-Nb-C ternary system, Journal de Physique IV (Proceedings), EDP sciences, 2004, pp. 35-39.

[29] F. Haddad, S.E. Amara, R. Kesri, Liquidus surface projection of the Fe-Nb-C system in the iron-rich corner, Metallurgical and Materials Transactions A, 39 (2008) 1026-1033.

[30] C. Raghunath, M. Bhat, P. Rohatgi, In situ technique for synthesizing Fe-TiC composites, Scripta metallurgica et materialia, 32 (1995) 577-582.

[31] A. Karantzalis, A. Lekatou, H. Mavros, Microstructural modifications of as-cast high-chromium white iron by heat treatment, Journal of materials engineering and performance, 18 (2009) 174-181.

[32] G. Powell, J. Bee, Secondary carbide precipitation in an 18 wt% Cr-1 wt% Mo white iron, Journal of materials Science, 31 (1996) 707-711.

[33] T. Fischer, Z. Zhu, H. Kim, D. Shin, Genesis and role of wear debris in sliding wear of ceramics, Wear, 245 (2000) 53-60.

[34] J. Lancaster, A review of the influence of environmental humidity and water on friction, lubrication and wear, Tribology International, 23 (1990) 371-389.

[35] K.-H. Zum Gahr, W.G. Scholz, Fracture toughness of white cast irons, JOM, 32 (1980) 38-44.

[36] M. Scanlan, D.J. Browne, A. Bates, New casting route to novel functionally gradient light alloys, Materials Science and Engineering: A, 413-414 (2005) 66-71.